Fast Ion Conductor Nanofibers and Aramid Nanofibers with Hydrogen Bonds Synergistically Enhanced Composite Solid Electrolytes

Hengying Xiang[1,2] · Lu Gao[1,2] · Dongjie Shi[3] · Long Jiao[5] · Bowen Cheng[1,2] · Nanping Deng[1,2] · Geng Li[4] · Weimin Kang[1,2]

Abstract

The low ionic conductivities, poor high-voltage stabilities, and lithium dendrite formation of polymer solid electrolytes preclude their use in all-solid-state lithium metal batteries (ASSLMBs). This work provides a simple and scalable technique for constructing fast ion conductor nanofibers (FICNFs) and poly-m-phenyleneisophthalamide (PMIA) nanofibers synergistically enhanced polyethylene oxide (PEO)-based composite solid electrolytes (CSEs) for ASSLMBs. The FICNFs, which were mainly composed of high loadings of ZrO_2 or $Li_{6.4}La_3Zr_{1.4}Ta_{0.6}O_{12}$ nanoparticles, had a percolated ceramic phase inside the nanofibers, while the exposed nanoparticles formed continuous organic–inorganic interfaces with the PEO matrix to enable Li^+ transport. The interfacial transport rate between ZrO_2 and PEO was calculated as 4.78×10^{-5} cm^2 s^{-1} with ab initio molecular dynamics (AIMD) simulations. Besides, the PMIA nanofibers provided strong skeletal support for the CSEs, ensuring excellent mechanical strength and safety for thin CSEs even at high temperatures. More importantly, the amide groups in PMIA provided abundant hydrogen bonds with TFSI$^-$, which lowered the lowest unoccupied molecular orbital (LUMO) level of lithium salts, thus promoting the generation of lithium fluoride-rich solid electrolyte interphase. Consequently, the modified CSEs exhibited satisfactory ionic conductivities (5.38×10^{-4} S cm^{-1} at 50 °C) and notable Li dendrite suppression (> 1500 h at 0.3 mAh cm^{-2}). The assembled LiFePO$_4$‖Li full cells display ultra-long cycles (> 2000 cycles) at 50 °C and 40 °C. More strikingly, the LiNi$_{0.8}$Mn$_{0.1}$Co$_{0.1}$O$_2$ (NMC811)‖Li cell also can stably run for 500 cycles, and the LiFePO$_4$‖Li flexible pouch cells also cycled normally, demonstrating tremendous potential for practical application.

Keywords Composite solid electrolytes · Multiple continuous Li$^+$ transmission channels · Rich hydrogen bond interactions · Ultra-long stable cycle performance · Flexible pouch cells

Introduction

All-solid-state LMBs (ASSLMBs) with high security and outstanding energy density are considered one of the next-generation rechargeable energy storage devices [1–3].

Solid-state electrolytes (SSEs), as one of the key components in ASSLMBs, usually have three categories: Inorganic solid electrolytes (ISEs), solid polymer electrolytes (SPEs), and composite solid electrolytes (CSEs) [4]. Qualified SSEs for ASSLMBs generally meet the following requirements:

✉ Nanping Deng
dengnanping@tiangong.edu.cn

✉ Geng Li
geng_li@regcc.cn

✉ Weimin Kang
kangweimin@tiangong.edu.cn

1 State Key Laboratory of Separation Membranes and Membrane Processes, Tiangong University, Tianjin 300387, China

2 School of Textile Science and Engineering, Tiangong University, Tianjin 300387, China

3 National Supercomputer Center in Tianjin, Tianjin 300457, China

4 China Rare Earth Group Research Institute, Ganzhou 341000, Jiangxi, China

5 State Key Laboratory of Biobased Fiber Manufacturing Technology, Tianjin Key Laboratory of Pulp and Paper, Tianjin University of Science and Technology, Tianjin 300457, China

First, SSEs not only have excellent ion conductivity ($> 10^{-4}$ S cm^{-1}) at room temperature, wide electrochemical window, and high Li-ion (Li$^+$) migration number, but also should be equipped with admirable mechanical strength to effectively inhibit lithium dendrite growth. Second, the interface between the cell electrode and electrolyte should have a low and stable impedance. Third, the overall processing performance should be outstanding, and mass production should be easy [4, 5].

Understanding lithium-ion transport is crucial for designing and optimizing highly ion-conductive SSEs, as conductivity is a key indicator of the SSE performance of ASSLMBs. In ISEs, lithium ions are usually transported in crystals by vacancy migration or ion hopping [6]. ISEs usually have excellent conductivity at room temperature (RT) [7]. For example, some sulfide-based ISEs, like the argyrodite family, demonstrate remarkably high ionic conductivities ranging from $\sim 10^{-3}$ to 10^{-2} S cm^{-1} at RT [8, 9]. Nevertheless, most of them are sensitive to H$_2$O and O$_2$ and have large contact resistance with cell electrodes. SPEs facilitate Li$^+$ conduction primarily in the amorphous phase of the polymer. Li$^+$ undergoes a "complexation-decomplexation-recomplexation" process, repeatedly jumping between different complexation sites as polymer chain segments move, thereby enabling long and fast-range Li$^+$ conduction [10]. SPEs are typically flexible and processable, providing better interfacial contact with electrodes compared to ISEs [11]. However, SPEs with poor strength cannot effectively prevent the growth of lithium dendrites during the cell cycle, and their ionic conductivity at RT generally is low due to sluggish polymer chain movement [12, 13].

As is known to all, the preparation of CSEs by dispersing inorganic fillers into polymers is one of the most effective ways to improve ionic conductivity, mechanical strength, and/or electrochemical stability [14]. The CSEs integrate the advantages of organic and inorganic materials while mitigating their disadvantages. The ion conduction mechanism of the prepared CSEs follows the percolation model [15, 16]. Below a certain ceramic content, lithium ions can only be conducted through the polymer matrix, resulting in low ion conductivity. However, once the ceramic content exceeds a certain point, lithium ions usually can also be conducted through ceramic particles or interfaces between organic and inorganic components, leading to significantly improved ionic conductivity [16, 17]. In addition, some studies also have found that the electrolyte conductivity was positively correlated with the number of interfaces, but not with the conductivity of the inorganic phase in high ceramic content CSEs (HCC CSEs). Furthermore, the conduction pathway primarily occurred at the interfaces between the ceramic and polymer phases in CSEs [18]. In this scenario, the ion conductivity of the ceramic phase became less important. As a result, low-cost insulating ceramics can be utilized as fillers

in SSEs, replacing expensive lithium-ion conductors. The substitution significantly reduces the overall cost of the SSEs without compromising their performance. However, in HCC CSEs, surface impurities in the ceramic phase, agglomeration of ceramic particles, and poor contact between ceramic particles and ceramic-polymer may lead to the room temperature conductivity of the CSEs being still low. Although introducing 3D ceramic nanofiber networks has proven to be a promising strategy to improve properties such as mechanical properties, ionic conductivity, and structural stability of solid electrolyte membranes, many technical challenges remain in the production and final use of nanofibers. Moreover, 3D ceramic nanofiber networks are usually can be prepared in various ways and then calcined at high temperatures, which are usually rather brittle and are difficult to use as a strong mechanical carrier in battery manufacturing and final application. Therefore, the development of CSEs with excellent ionic conductivity and outstanding mechanical strength still is the key to promoting the fast development of CSEs for ASSLMBs.

Due to its high permittivity, strong solvation ability of Li$^+$, and good molecular chain flexibility, polyethylene oxide (PEO) is widely used as the matrix of the CSEs [19]. Nevertheless, ionic conductivities (σ) of PEO-based electrolytes at RT typically range from 10^{-7} to 10^{-5} S cm^{-1}, which falls below the requirement for ASSLMBs. Besides, pure PEO SPEs also have a narrow electrochemical window (about 3.8 V) and weak mechanical properties, leading to difficulty with high voltage cathodes such as LiNi$_{0.8}$Mn$_{0.1}$Co$_{0.1}$O$_2$ (NMC811), causing serious safety hazards, and blocking its practical application [20]. Given the intractable problems of PEO SPEs, the introduction of a three-dimensional organic high-strength nanofiber membrane is one of the effective methods to improve its mechanical properties. When compared with nanofibers prepared by other processes, electrospun nanofibers usually have attracted widespread attention because of their remarkable mechanical properties, high porosities, and large surface area-to-volume ratios [21]. The SPEs with some electrospun nanofibers as supporting skeletons still have a thin thickness with excellent mechanical strength conditions, which can significantly improve the overall energy density of the battery [22]. At the same time, it has also been reported that different hydrogen bond interactions in electrolytes can not only increase the oxidation potential of SPEs [23], but also promote the dissociation of lithium salts and the generation of lithium fluoride (LiF)-rich solid electrolyte interphase (SEI) [24, 25]. Lastly, the utilization of cost-effective electrolytes is of utmost importance for advanced ASSLMBs to fulfill the demands of large-scale energy storage applications. Therefore, scalable electrospinning membranes also can provide strong technical support for the integration of large-scale nanofiber membranes into polymer electrolytes.

Based on the above basic research and discussions, we have innovatively designed and prepared the functional composite nanofiber membranes (CNMs) by scalable electrospinning, which was composed of high-content ceramic nanoparticle reinforced nanofiber called fast ion conductor nanofibers (FICNFs) and poly-m-phenyleneisophthalamide (PMIA) nanofiber as the supporting skeleton of PEO-based electrolyte with thin thickness (Fig. 1a). A percolated ceramic phase was formed inside the prepared FICNFs,

in which PEO served as the binder for high-load ZrO_2 or $Li_{6.4}La_3Zr_{1.4}Ta_{0.6}O_{12}$ (LLZTO) nanoparticles, while the exposed ceramic nanoparticles outside the nanofibers formed continuous organic–inorganic interfaces for Li^+ transport in the CSEs. The result allows Li^+ to be transported not only rapidly within the nanofibers but also along the interfaces, providing multiple Li^+ transport channels in the CSEs (Fig. 1b), which has been confirmed by ab initio molecular dynamics (AIMD) simulation. Besides, the PMIA nanofibers
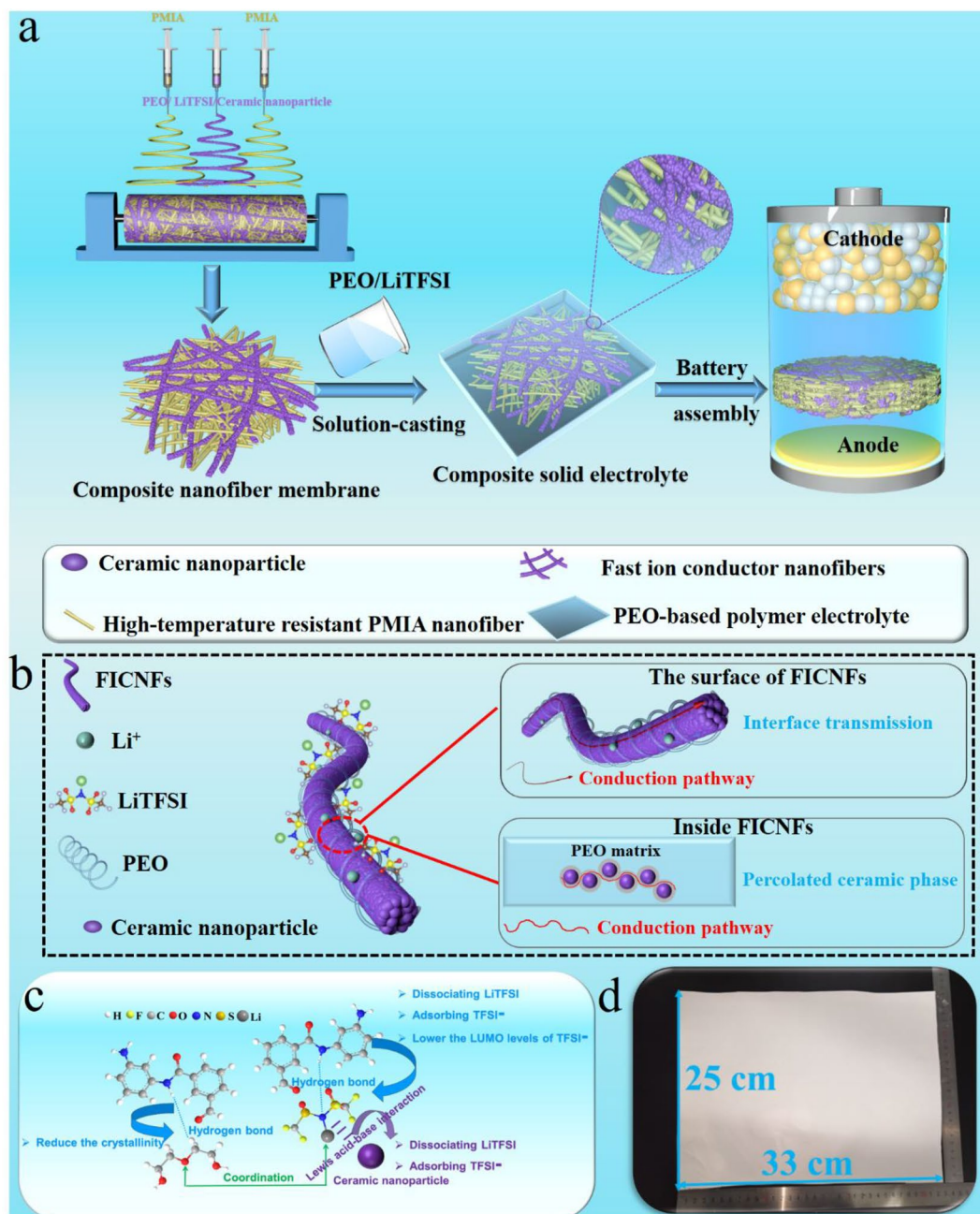

Fig. 1 **a** The schematic illustration for the preparation processes of the CSEs and assembled ASSLMBs using the CSEs. **b** Mechanism for enhanced Li^+ transport by FICNFs. **c** Various interactions of the electrolyte. **d** PMIA&Z60 nanofiber membrane

furnished strong skeleton support to ensure the thin CSEs with outstanding mechanical strength and high-temperature resistance. The characterization tests and density functional theory (DFT) calculations also have verified that enough hydrogen bonding interactions between the amide groups in the PMIA and PEO can reduce the crystallinity and enhance the oxidation resistance of PEO. These hydrogen bond interactions with TFSI$^-$ not only promoted the dissociation of lithium salts but also facilitated the generation of LiF-rich SEI (Fig. 1c). The CSEs prepared simultaneously solve the problem of unsatisfactory ion conductivity, poor thermal stability, weak suppression of lithium dendrites and low oxidation potential of PEO-based electrolytes. Therefore, the optimized CSEs, when used in Li‖Li symmetric cells, exhibited remarkable cycle stability (> 1500 h at 0.3 mAh cm^{-2}). Furthermore, the LiFePO$_4$|CSEs|Li batteries displayed ultra-long cycles (> 2000 cycles). Additionally, when employed in Li‖NMC811 batteries, the prepared CSEs enable stable operation at a high cut-off voltage of 4.3 V for 500 cycles at 0.3 C. Notably, the pouch cells also demonstrated stable operation, exceptional flexibility, and outstanding safety, making them highly suitable for potential practical applications.

Experimental Section

For simplicity, the prepared PMIA nanofibers membrane was denoted as PMIA, and the FICNFs prepared with a ratio of 15 wt%, 30 wt%, 45 wt%, 60 wt%, and 75 wt% of ZrO$_2$ nanoparticle in whole solutes (ZrO$_2$, PEO, and lithium bis(trifluoromethanesulfonyl)imide (LiTFSI)) were labeled as Z15, Z30, Z45, Z60, and Z75, respectively. The FICNFs prepared with a ratio of 60 wt% LLZTO nanoparticle in whole solutes (LLZTO, PEO, and LiTFSI) were labeled as L60. The composite fiber membranes consist of PMIA nanofibers and different ZrO$_2$ content of FICNFs were labeled as PMIA&ZX (X was the proportion of ZrO$_2$ to the total solute). The composite fiber membrane consists of PMIA nanofibers and L60 nanofibers were labeled as PMIA&L60. Besides, the all-solid-state CSEs prepared using pure PEO and LiTFSI solution, PEO, x wt% ZrO$_2$ nanoparticles (x was the mass percentage of the solute), and LiTFSI mixture solution, PMIA nanofiber membrane pouring PEO solution, PMIA&ZX nanofiber membrane pouring PEO solution, PMIA&Z60 membrane pouring PEO and 10 wt% ZrO$_2$ nanoparticles mixture solution, PMIA&L60 membrane pouring PEO were denoted as PEO, PEO/xZ, PEO/PMIA, PMIA&ZX, PEO/10Z/PMIA&Z60, and PEO/PMIA&L60 electrolytes, respectively. The other details for the experimental section were fully introduced and presented in the Supporting Information.

Results and Discussion

The preparation processes of CSEs and the assembly processes of ASSLMBs are illustrated in Fig. 1a. Firstly, a composite membrane containing the FICNFs and PMIA nanofibers rich in amide bonds was prepared in the scalable electrospinning way. Then the PEO base CSEs were prepared by the solution pouring method. As shown in Fig. 1d, the size of the electrospinning PMIA&Z60 composite membrane can reach 33 cm × 25 cm, which meets the requirements of large-scale energy storage applications and flexible electrolytes.

Building on our previous works, the PMIA nanofiber membrane was successfully prepared as shown in Fig. 2a, which was composed of uniform nanofibers. Subsequently, we intend to introduce continuous FICNFs into these prepared nanofiber membranes. Figures 2b and S1a–d display the morphologies of electrospun CNMs with different contents of ZrO$_2$ nanoparticles. When the contents of solvent, PEO, and lithium salt are fixed, the PEO-based spinning solution tends to be fibrous with the increase of ZrO$_2$ nanoparticles. However, no continuous percolated ceramic phase can be formed. When the proportion of ZrO$_2$ accounted for 60 wt% of the solute, the nanofibers were continuous and there was no bulk aggregation. The detailed morphology of ZrO$_2$-based nanofiber with an average diameter of about 600 nm was characterized by a TEM test. As shown in Fig. 2c, PEO served as a binder to interconnect the ZrO$_2$ nanoparticles, and the well-distributed Zr and O elements (Fig. 2d) also demonstrated that ZrO$_2$ was evenly dispersed in the nanofibers to form an obvious percolated ceramic phase and continuous ion transport paths at the organic/ceramic interfaces. However, as the proportion of ZrO$_2$ was increased, the nanofibers appeared ZrO$_2$ aggregation, which was not conducive to the rapid transport of the lithium ions. The above phenomenon may be explained that when the ZrO$_2$ nanoparticles content was less than 60 wt%, the solute PEO in the spinning solution accounts for the majority. While the excessive solvent made PEO directly sprayed onto the PMIA nanofiber membrane in the form of the solution instead of nanofiber. When the ZrO$_2$ content was increased to 60 wt%, the ZrO$_2$ in this spinning solution accounted for the majority, and the most appropriate ratio between solvent and solute in the solution was reached. Under the action of the electrostatic field, PEO can act as a binder to make ZrO$_2$ orderly and arrange into continuous nanofibers. Interestingly, with the same preparation method, we also prepared continuous nanofibers containing high loads and evenly distributed LLZTO nanoparticles (60 wt% LLZTO) with an average diameter of approximately 800 nm (Fig. 2e–g), which effectively proved that this method
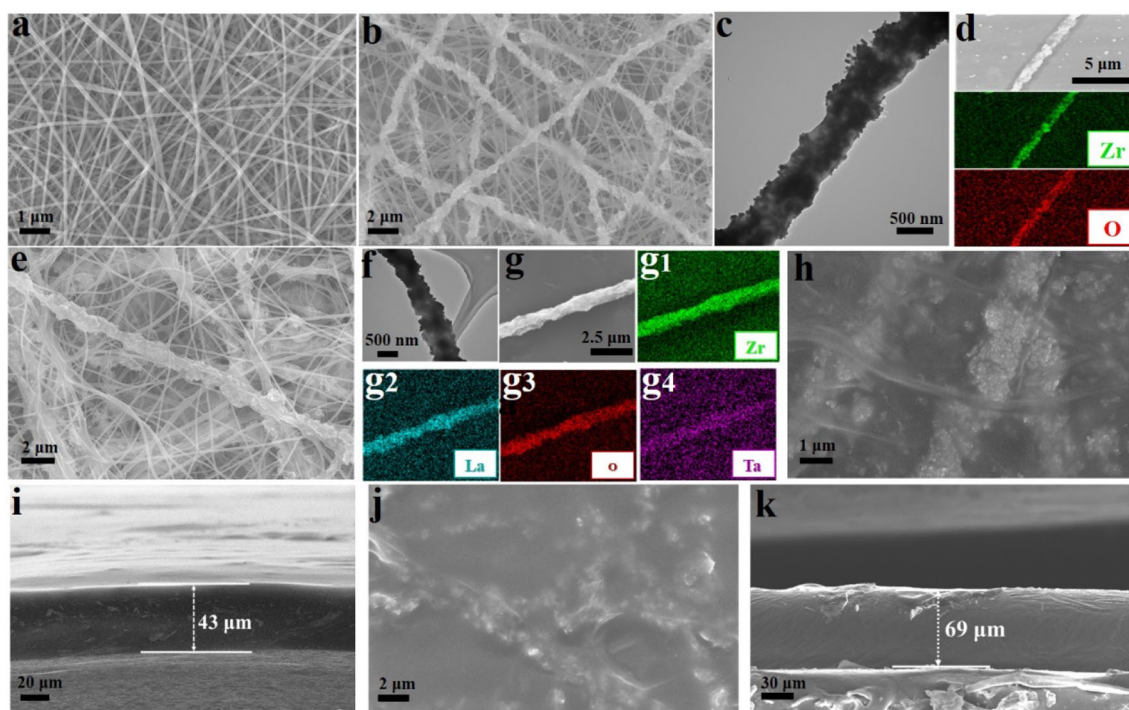
Fig. 2 SEM images of **a** PMIA nanofiber membrane; **b** PMIA&Z60 nanofiber membrane; **c** TEM image of Z60 nanofiber; **d** EDX mapping images of Z60 nanofiber; **e** SEM images of PMIA&L60; **f** TEM image of L60 nanofiber; **g** EDX mapping images of L60 nanofiber: g_1 Zr elements, g_2 La elements, g_3 O elements, g_4 Ta elements; **h** The top-view SEM image and **i** the cross-section SEM image of PEO/10Z/PMIA&Z60 CSEs; **j** The top-view SEM image and **k** the cross-section SEM image of PEO/PMIA&L60 CSEs

was useful for the preparation of continuous nanofibers with high loads of ceramic nanoparticles. The top-view SEM images of CSEs in Fig. 2h and j represent a flat and smooth surface morphology, revealing the pores in the PMIA&Z60 and PMIA&L60 composite membranes have been evenly filled by the PEO-based electrolyte. In addition, it can be seen from the EDS test in Fig. S2 that Zr and O were evenly dispersed in the electrolyte, indicating the successful addition of PMIA&Z60 composite membranes and ZrO_2 nanoparticles. According to the cross-sectional SEM images of CSEs in Fig. 2i–k and compared with the cross-sectional SEM images of PEO electrolyte (Fig. S3), the thickness of CSEs was lower than 43 μm and 65 μm, respectively, due to the excellent mechanical properties of the CNMs.

Adding nano-fillers to the PEO polymer can significantly inhibit the crystallization of the PEO chain dynamically due to the strong Lewis acid–base type interaction between the surface of the nanoparticles and the PEO chain [26, 27]. Based on this, we have added ZrO_2 nanoparticles to the PEO-based electrolyte and found that reducing the crystallinity of PEO reached the optimal level when the addition amount was 10 wt% (Fig. S4). Furthermore, with the addition of multi-level PMIA to the pure PEO electrolyte, the two characteristic peaks of PEO (19.3° and 23.6°) also became

significantly smaller. The nanofillers with high specific surface area can produce more interfacial layers and form ion transport networks. However, the aggregation of nanofillers can destroy the percolation path along the interface layer. To fully utilize the interface layer, a continuous nanofiber containing high-content inorganic ceramic nanoparticles can be introduced to form a continuous interface layer [28]. Therefore, as can be seen from Fig. 3a, we have introduced the PMIA&Z60 nanofibers into the PEO/10Z electrolyte, resulting in the formation of a continuous percolative network in the composite electrolyte without agglomeration. Moreover, the introduction of PMIA&L60 nanofibers membrane into the PEO electrolyte also formed a continuous percolative network without agglomeration.

Some studies have shown that reducing the crystallization of polymer chains can enhance the movement of chain segments and effectively promote the transport of lithium ions. In addition, the Lewis acid–base interaction also promoted the dissociation of Li salts, increased the concentration of free Li^+ near the interfaces, and further improved the transportation of lithium ions. Figures 3b and S5 present the Arrhenius plots for various electrolytes at different temperatures from 30 to 70 °C. Figure S5 shows that when ZrO_2 was added to the PEO, the ionic conductivity of the CSE initially increased and then decreased due to agglomeration
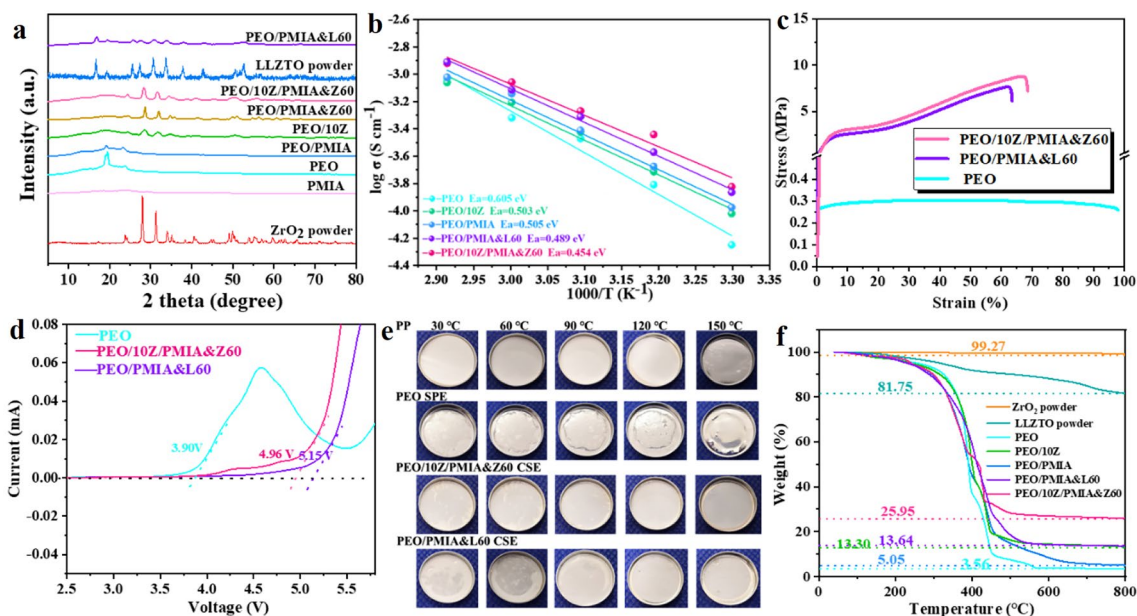
Fig. 3 **a** XRD patterns. **b** Arrhenius plots (temperature increased from 30 to 70 °C). **c** Stress–strain profiles. **d** LSV images of different electrolytes. **e** Optical images of various films treated at different temperatures for 60 min. **f** TGA measurements of various samples

of the excess ZrO$_2$ nanoparticles. The ionic conductivity reached a maximum when 10 wt% of the ZrO$_2$ nanoparticles was added. Furthermore, Fig. 3b also shows that the introduction of the PMIA nanofiber membrane increased the ionic conductivity of the electrolyte. The main reason was that excess hydrogen bonding interactions between the meta-type benzene-amide bonds on the PMIA skeleton chain and PEO and LiTFSI may hinder polymer crystallization and cause the decomposition of LiTFSI. Moreover, the PEO/PMIA&L60 and PEO/10Z/PMIA&Z60 CSEs also presented admirable ionic conductivity. Those results displayed that the ionic conductivity of all CSEs was higher than that of the PEO SPE at the temperature range of 30–70 °C. The corresponding ionic conductivities of the PEO/10Z, PEO/PMIA, PEO/PMIA&L60, and PEO/10Z/PMIA&Z60 CSEs are 9.56×10^{-5} S cm^{-1}, 1.06×10^{-4} S cm^{-1}, 1.37×10^{-4} S cm^{-1} and 1.5×10^{-4} S cm^{-1} at 30 °C, respectively, which was significantly higher than 5.63×10^{-5} S cm^{-1} of the PEO electrolyte. Meanwhile, the ion conductivity data at different temperatures were fitted and the results showed that the relationship between ion conductivity and temperature follows the classical Arrhenius equation (Eq. 1):

$$\sigma = A \exp\left(-\frac{E_a}{RT}\right) \tag{1}$$

where A, E_a, R, and T represent the pre-exponential factor, activation energy, gas constant (8.314 J mol^{-1} K^{-1}), and absolute temperature, respectively [29, 30]. The calculated activation energies of PEO/PMIA&L60 and PEO/10Z/

PMIA&Z60 CSEs were 0.489 eV and 0.454 eV, respectively, which were significantly lower than PEO SPE ($E_a = 0.605$ eV), as well as PEO/10Z ($E_a = 0.503$ eV) and PEO/PMIA ($E_a = 0.505$ eV), indicating that the synergistic effect between FICNFs and PMIA nanofibers promotes faster ion migration in the electrolyte. The specific reasons for these improvements in the ionic conductivity were: (1) introduction of the -NH group in PMIA led to Li…N–H interactions in the system, which had a binding energy equivalent to that of Li…O–C, thus promoting the destruction and formation of coordination bonds between the polymer and lithium ions [31]; (2) the hydrogen bond interactions between PMIA and PEO and TFSI⁻ greatly reduced the crystallinity of PEO and promoted the dissociation of lithium salt; (3) The interfaces exist within FICNFs with percolated networks, or between the inorganic ceramic nanoparticles exposed on the surface of FICNFs and the filled PEO also can provide rich transport pathways, thereby improving Li⁺ transport.

The tensile strengths of PEO/10Z/PMIA&Z60 and PEO/PMIA&L60 CSEs were investigated and presented by the stress–strain profiles (Fig. 3c). When compared to PEO electrolytes (≈ 0.30 MPa), the mechanical properties of PEO/10Z/PMIA&Z60 (8.76 MPa) and PEO/PMIA&L60 (7.75 MPa) CSEs have been significantly improved. The satisfactory results mainly involved the strong interaction between nanofibers in these PMIA nanofiber membranes through binding points and entanglement, thereby improving the overall mechanical strengths of CSEs. In addition, enough hydrogen bonding interactions between PMIA

and PEO molecules were also beneficial for the excellent mechanical properties of the prepared composite electrolytes [32].

The electrochemical stability window (ESW) of diverse electrolytes, as an essential criterion for their application in high-voltage batteries, was evaluated at 50 °C by the linear sweep voltammetry (LSV) from 2.5 to 6.0 V. As shown in Fig. 3d, the ESW of the PEO/10Z/PMIA&Z60 (4.96 V vs. Li^+/Li) and PEO/PMIA&L60 (5.15 V vs. Li^+/Li) CSEs were all much wider than that of PEO (3.90 V vs. Li^+/Li), which indicated that the introduction of the PMIA&Z60 and PMIA&L60 nanofiber network can effectively enhance the ESW of CSEs. The increase in ESW may be due to the addition of PMIA, ZrO_2, and LLZTO with good oxidation stability [33]. The irreversible oxidation of bis (trifluoromethane sulfonimide) ($TFSI^-$) would seriously reduce the antioxidant stability of PEO. The strong Lewis acid–base interaction between the acid sites on the surface of ceramic particles (ZrO_2 and LLZTO) and salt anions can effectively inhibit the migration of $TFSI^-$, thus improving the electrochemical stability of the composite electrolyte [34]. In addition, the highly interconnected PMIA&Z60, and PMIA&L60 nanofiber network also can provide continuous ion transport pathways, which greatly reduces the migration of charges (i.e. Li^+) in the PEO polymer matrix, thereby delaying the oxidation of PEO [35].

In safety evaluation, the thermal stability of the SPE structure is a very important indicator for high-safety lithium batteries [36]. Figure 3e shows the photos of different SPEs tested at various temperatures for 60 min. With the increase in temperature, the PP membrane, PEO, and PEO/10Z electrolyte membrane gradually shrink, especially at high temperatures. However, thanks to the outstanding heat resistance of PMIA itself [37], the PMIA nanofiber membrane introduced electrolytes all remained a regular and complete morphology, which just has negligible shrinkage after being treated for 60 min at 150 °C.

Thermogravimetric analysis (TGA) results for the samples were obtained in air, as shown in Fig. 3f. It can be seen that the thermal decomposition trend of several composite electrolytes was similar to PEO electrolytes. The thermal decomposition process of PEO-based electrolytes can be divided into two stages. The first stage occurred at 60–160 °C, which was the thermal decomposition process of a small amount of water and residual solvent in the electrolyte. The other stage occurred at 380–500 °C, which was mainly due to the decomposition of PEO [38]. In addition, when the temperature reached 800 °C, it was obvious that the participation amount of PEO, PEO/10Z, PEO/PMIA&L60 CSEs, and PEO/10Z/PMIA&Z60 was nearly 3.56 wt%, 13.30 wt%, 13.64 wt%, and 25.95 wt%.

Finally, visual experiments were carried out on the samples with different electrolyte strip sizes, which verified

the improved flame retardancies of the samples containing the PMIA&Z60 and PMIA&L60 nanofiber membranes. Figure S6 shows a number of screenshots of electrolyte combustion at different time points. When the high-temperature flame approached, the PEO and PEO/10Z solid electrolyte samples burned continuously and produced droplets, which is typical of polymer combustion, and they were almost completely burned within 8 s. Nevertheless, the PEO/10Z/PMIA&Z60 and PEO/PMIA&L60 CSEs introduced into the PMIA nanofiber membrane exhibited shrinkage without burning when the flame was closed. The evident fire-extinguishing behavior constituted an improvement in the battery performance even at high temperatures and was also an important guarantee for future applications.

Finally, some visual experiments were carried out on the samples with different electrolyte strip samples, which verified the improvement of the flame retardancy of the samples by introducing PMIA&Z60 and PMIA&L60 nanofiber membranes. Figure S6 presents a combination of screenshots of the electrolyte's combustion state at different time points. It can be seen that when the high-temperature flame approached, the PEO and PEO/10Z solid electrolyte samples burned continuously, accompanied by droplet drop, which was typical of polymer combustion, and finally almost completely burned within 8 s. Nevertheless, the PEO/10Z/PMIA&Z60 and PEO/PMIA&L60 CSEs introduced into the PMIA nanofiber membrane just had a certain shrinkage without burning when the high-temperature flame was close to it. The evident fire-extinguishing behavior was an effective way to improve the performance of batteries even at high temperatures, and also an important guarantee for future applications.

The Li^+ transference number (t_{Li}^+) is a significant factor in valuing the Li^+ migration ability in SPEs. Higher $t_{Li}+$ has a positive role in diminishing polarization and restraining side reactions [39]. The t_{Li}^+ of PEO SPE, PEO/10Z/PMIA&Z60, and PEO/PMIA&L60 CSEs can be calculated based on the AC impedance and chronoamperometry profiles polarization. As shown in Fig. 4a, b, the t_{Li}^+ of the PEO/10Z/PMIA&Z60 and PEO/PMIA&L60 CSEs were calculated to be 0.45 and 0.42, respectively, which were both higher than that of the PEO SPE (0.13) as presented in Fig. S7. The notable improvements in Li^+ transport by the PEO/10Z/PMIA&Z60 and PEO/PMIA&L60 CSEs were attributed to the: (1) the hydrogen bonding interactions between the PMIA nanofibers and $TFSI^-$ led to adsorption of the $TFSI^-$ and dissociation of the salts; (2) the ceramic nanoparticles acted as Lewis acids and the $TFSI^-$ Lewis bases were absorbed on the surfaces of the ceramic nanoparticles; and (3) the applied FICNFs provided multiple continuous Li^+ transport pathways and contributed to rapid Li^+ migration.
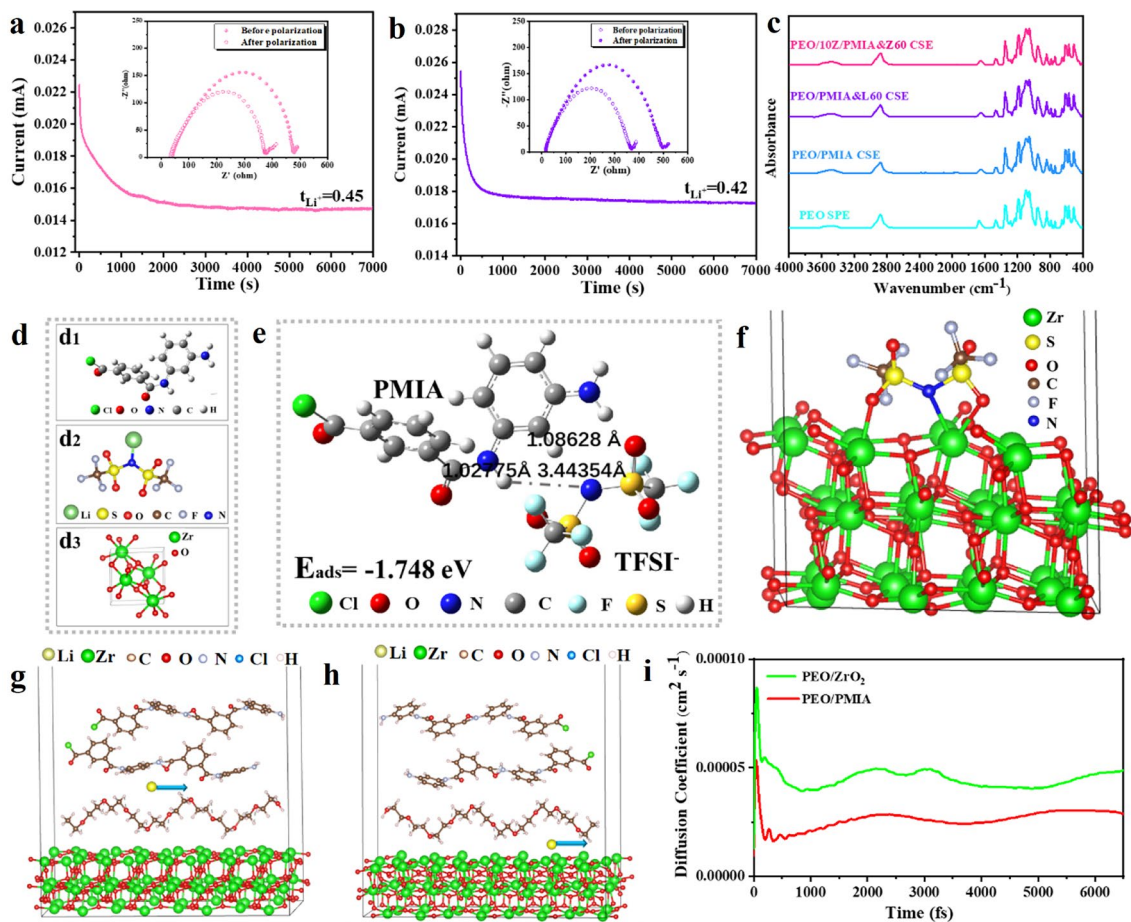
Fig. 4 Chronoamperometry profiles for Li symmetric cells with **a** PEO/10Z/PMIA&Z60 and **b** PEO/PMIA&L60 CSEs (the inset presents the impedance changes before and after polarization). **c** FTIR spectra of PEO SPE, PEO/PMIA, PEO/PMIA&L60, and PEO/10Z/PMIA&Z60 CSEs at 4000 to 400 cm^{-1}. **d** Molecular structures of **d$_1$** PMIA, **d$_2$** LiTFSI and **d$_3$** ZrO$_2$. **e** Detailed hydrogen bond of PMIA with TFSI$^-$. **f** Stable configuration of TFSI$^-$ absorbed on the (– 111) plane of ZrO$_2$. Schematic diagram of lithium-ion diffusion path at **g** PEO/PMIA and **h** PEO/ZrO$_2$; and **i** its corresponding diffusion rate

Figure 4c displays the FTIR spectra for PEO SPE, PEO/PMIA, PEO/10Z/PMIA&Z60, and PEO/PMIA&L60 CSEs in the range of 4000–400 cm^{-1}. To better observe the small differences caused by the addition of PMIA, PMIA&Z60, and PMIA&L60 nanofiber membrane to the PEO/LiTFSI matrix, the deconvoluted FTIR spectra in Fig. S8 present stretching vibrational modes of the C–O–C, –SO$_2$, and –CF$_3$ group in the frequency ranges 1160 to 1000 cm^{-1} and 1400 to 1150 cm^{-1}, respectively. When compared to the C–O–C characteristic peaks of PEO electrolyte [40] (1041.70, 1077.11, 1098.49, 1119.40, and 1144.78 cm^{-1}, respectively), the prepared PEO/PMIA, PEO/10Z/PMIA&Z60, and PEO/PMIA&L60 CSEs all have undergone a certain degree of deviation. The evolution of this C–O–C characteristic peak indicated a change in the chemical environment of the -EO group in PEO, further proving the interactions between C–O–C and PMIA as well as ZrO$_2$ and LLZTO nanofillers [41]. Furthermore, in the 1400 to 1150 cm^{-1} range, after

introducing PMIA, PMIA&Z60, or PMIA&L60 membrane to the PEO SPE, the -SO$_2$ stretching corresponding to the peaks at 1333.90 and 1302.47 cm^{-1} shifted to varying degrees, respectively. The –CF$_3$ symmetric stretching corresponding to the peaks at 1254.07 and 1227.65 cm^{-1}, and the –CF$_3$ asymmetric stretching corresponding to the peaks at 1194.48 and 1178.88 cm^{-1} all shifted to varying degrees, respectively. These shifts –SO$_2$ and –CF$_3$ groups indicated that the prepared PMIA, PMIA&Z60, and PMIA&L60 all have strong interactions with TFSI$^-$ anions, which effectively promoted the dissociation of LiTFSI and release more lithium ions [42].

The above basic characterization demonstrated that the prepared PEO/10Z/PMIA&Z60 and PEO/PMIA&L60 CSEs had high ion transport efficiency. To further investigate the reasons, the atomic scale DFT calculation was used to explain their relationship with Li$^+$ rapid motion. Here, we performed relevant calculations on PEO/10Z/

PMIA&Z60 CSEs as an example. The molecular structure of PMIA, ZrO$_2$, and LiTFSI was established in Fig. 4d. As shown in Fig. 4e, the local intermolecular interactions of hydrogen bonds with spacing 3.443 Å can be formed by the H atoms on the N–H group in the PMIA and N atoms in the TFSI$^-$. The adsorption energy (E_{ads}) of the PMIA molecule for TFSI$^-$ was – 1.748 eV, indicating satisfying adsorption capacity. Besides, the TFSI$^-$ was adsorbed on the (– 111) surface in the applied ZrO$_2$ (Fig. 4f). The results revealed that the E_{ads} of ZrO$_2$ for TFSI$^-$ was – 5.684 eV, which can effectively promote the dissociation of LiTFSI and facilitate the release of free Li$^+$ concentrated near the applied ZrO$_2$, thereby fully utilizing the rapid transfer of lithium ions at the polymer/ZrO$_2$ and polymer/LLZTO interfaces. Some studies also have shown that amorphous-rich zones occurred around inorganic fillers which allowed for rapid transfer of Li$^+$, which was mainly caused by polymer chains being fixed to the surface of ceramic fillers by physical and/or chemical action [43, 44]. Therefore, to further understand the motion of these free Li$^+$ in these CSEs, the transport velocities of Li$^+$ at the interfaces of PEO/PMIA and PEO/10Z/PMIA&Z60 CSEs were calculated adopting the AIMD simulations. Models of lithium ions between PEO and PMIA, and PEO and ZrO$_2$ were established (Fig. 4g, h), respectively. The (– 111) crystal plane of ZrO$_2$ was still used as the calculation object, and the temperature was set at 50 °C. Lithium ions ran for 6500 fs in the two interfaces. As shown in Fig. 4i, in the whole interfaces of PEO/PMIA and PEO/ZrO$_2$, the Li$^+$ diffusion rate can reach the highest 5.28×10^{-5} cm^2 s^{-1} and 8.62×10^{-5} cm^2 s^{-1}, respectively. After the threshold, the rate of Li$^+$ at the PEO/PMIA and PEO/ZrO$_2$ interface remained stable, maintaining around 3.08×10^{-5} cm^2 s^{-1}, and 4.78×10^{-5} cm^2 s^{-1}, respectively. The above calculation results directly emphasized the role of various interfaces existing in the PEO/10Z/PMIA&Z60 CSEs in facilitating the fast transport for Li$^+$. Therefore, based on the above characterization and corresponding theoretical calculations, it can be concluded that the remarkable improvement in ion transport efficiency of PEO/10Z/PMIA&Z60 and PEO/PMIA&L60 CSEs depended on the use of ion-regulated ZrO$_2$ nanoparticle, PMIA nanofiber, and FICNFs, which can also be extended to other types of solid electrolytes for their universalities.

The critical current density (CCD) is defined as the current density that causes the Li dendrites to grow through SEI and SSE and short-circuit the battery [45, 46]. The symmetrical Li‖Li batteries with different electrolytes by galvanostatic cycling with stepping the current density from 0.05 to 0.60 mA cm^{-2} at 50 °C were tested to evaluate their CCD. As shown in Figs. 5a–c and S9a–b, the CCD of the PEO electrolyte (Fig. S9a) and PEO/10Z (Fig. S9b) was 0.2 mA cm^{-2} and 0.4 mA cm^{-2}, respectively, where a short circuit occurred. Surprisingly, the CCD of all CSEs

containing the prepared PMIA nanofiber membranes had been significantly improved to 0.6 mA cm^{-2} (Fig. 5a–c). Especially, the CCD of the PEO/10Z/PMIA&Z60 and PEO/PMIA&L60 CSEs displayed a smoother voltage profile than that of the PEO/PMIA, demonstrating the effectiveness of FICNFs in the uniform deposition of lithium ions.

The constant discharge/charge voltage profiles of different symmetric Li‖SPEs‖Li batteries were also tested to examine the plating/stripping behavior and cycle stability of lithium as present in Figs. 5d and S10a–d. At first, all the Li‖SPEs‖Li batteries were charged and discharged for 10 h at current densities of 0.1, 0.2, 0.3, 0.4, and 0.5 mA cm^{-2} with the areal capacity of 0.1 mAh cm^{-2} at 50 °C. Noticeably, even at a high rate of 0.5 mA cm^{-2}, the assembled Li‖PEO/10Z‖Li, Li‖PMIA‖Li, Li‖ PEO/10Z/PMIA&Z60‖Li, and Li‖PEO/PMIA&L60‖Li symmetric batteries all displayed low polarization voltages and revealed the formation of a stable plating/peeling process. Contrastively, the assembled Li‖PEO‖Li battery caused a short circuit when the current density increased to 0.5 mA cm^{-2} (Fig. S10d). Subsequently, the current density returned to 0.2 mA cm^{-2} with the areal capacity of 0.1 mAh cm^{-2} again. As shown in Fig. S10c, Li‖PEO/10Z‖Li battery occurred hard short after 300 h because of overgrowth of the lithium dendrites. As for the Li‖PMIA‖Li battery, a short circuit just occurred when the stable cycle reached about as long as 1200 h (Fig. S10b). Moreover, the Li‖PEO/PMIA&L60‖Li battery had a stable cycle reached 1400 h without short-circuit (Fig. S10a). Amazingly, the Li‖PEO/10Z/PMIA&Z60‖Li can represent excellent stability and a smooth voltage platform for as long as 3700 h. Besides, even at a higher areal capacity of 0.3 mAh cm^{-2}, they can still cycle stable for 1500 h (Fig. 5e).

To fully demonstrate the resistance of the SPEs to lithium dendrites, the Li‖Li cells assembled with PEO and PEO/10Z/PMIA&Z60 SPEs continuously plated lithium at one interface testing a current density of 0.2 mA cm^{-2} at 50 °C were established (Fig. 6a). The test results showed that the Li‖PEO/10Z/PMIA&Z60‖Li cells can sustain 100 h. In addition, an in situ optical microscope was used to track and observe the changes in the cross-section interface of Li‖PEO/10Z/PMIA&Z60‖Li cells during lithium deposition, it was found that PEO/10Z/PMIA&Z60 CSEs can effectively maintain a good interface, and dense and uniform lithium deposition (Fig. 6d). However, Li‖PEO‖Li cell was short-circuited only after plating for 6 h, which was mainly due to the obvious dendrite growth that began to appear after half an hour as shown in Fig. 6c. The above dramatic contrast results demonstrated that the prepared PMIA&Z60 nanofiber membranes played an important role in improving the resistance of electrolytes to lithium dendrites. Stress on the electrolyte caused by some severe lithium dendrites can cause damage and cracks within the electrolyte [47, 48]. Therefore, CSEs containing PMIA&Z60 nanofibers
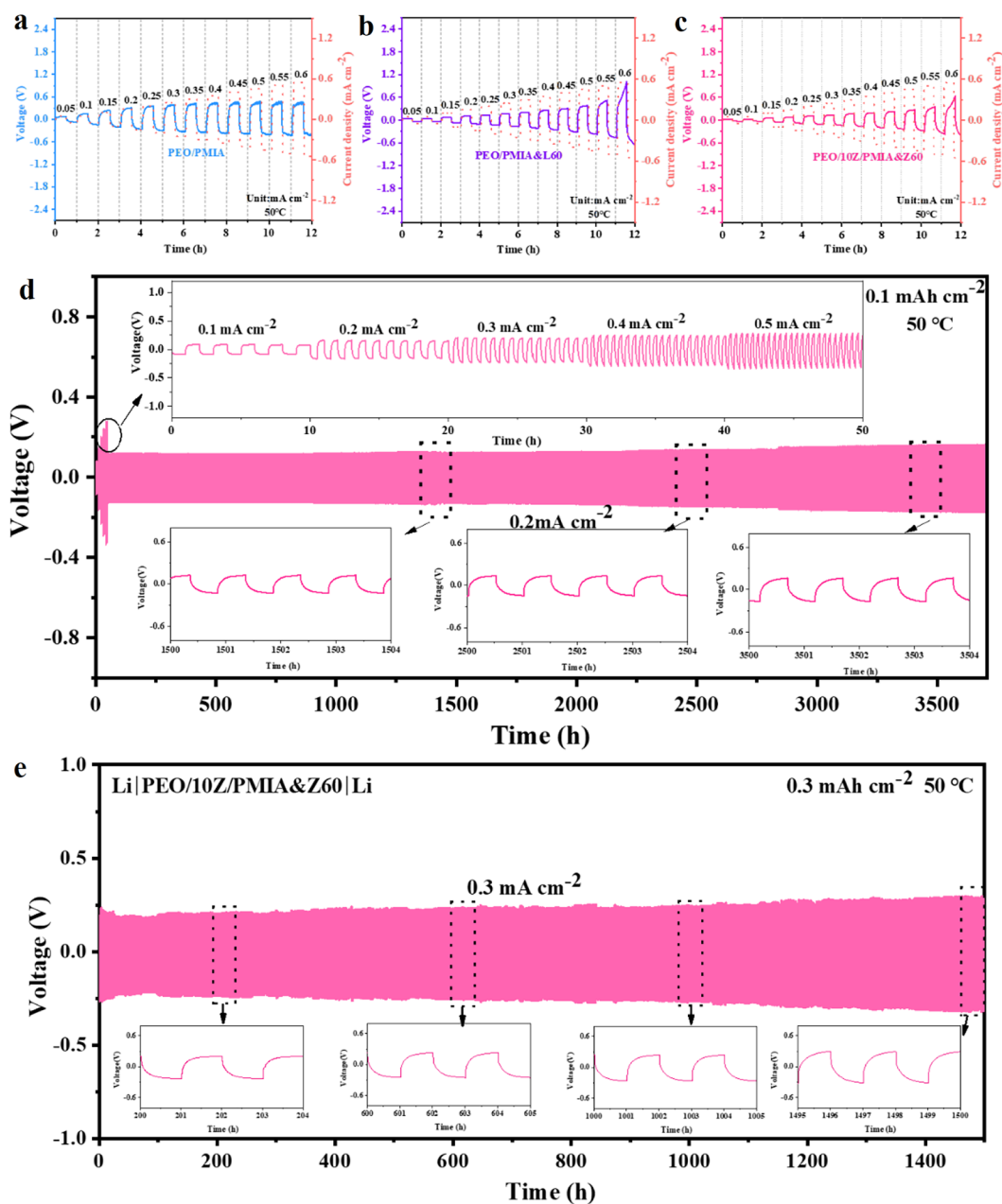
Fig. 5 **a–c** The critical current density of different CSEs at 50 °C. **d** The cycling performance of the Li|Li symmetric battery with PEO/10Z/PMIA&Z60 CSEs at different current densities with a constant capacity of 0.1 mAh cm^{-2} at 50 °C. **e** The cycling performance of the Li|Li symmetric battery with PEO/10Z/PMIA&Z60 CSE under 50 °C at the current density of 0.3 mA cm^{-2} for 0.3 mAh cm^{-2}

membrane can resist to some extent the damage caused by anisotropic stress and separation displacement fields caused by lithium dendrites due to their high mechanical strength. The Li|PEO/10Z/PMIA&Z60|Li and Li|PEO|Li symmetric cells were also tested by the galvanostatic intermittent titration technique (GITT) at 0.2 mA cm^{-2} and 50 °C to highlight the better Li$^+$ mobility through PEO/10Z/PMIA&Z60 CSEs when compared with other samples (Fig. 6b). A limited Li plating (charge/discharge for 20 s) was applied to

the electrode, and then the battery was stationary for 180 s to achieve a balanced state, which was a periodical GITT process. Through the GITT test, the Li$^+$ concentration effect was minimized, while the electrode kinetic effect was maximized [41]. It can be seen from the GITT results that the Li|PEO|Li battery short-circuited during the test, and its overpotential (about 330 mV) was much larger than that of the Li|PEO/10Z/PMIA&Z60|Li cell (about 99 mV). The simultaneous introduction of FICNFs and PMIA nanofibers
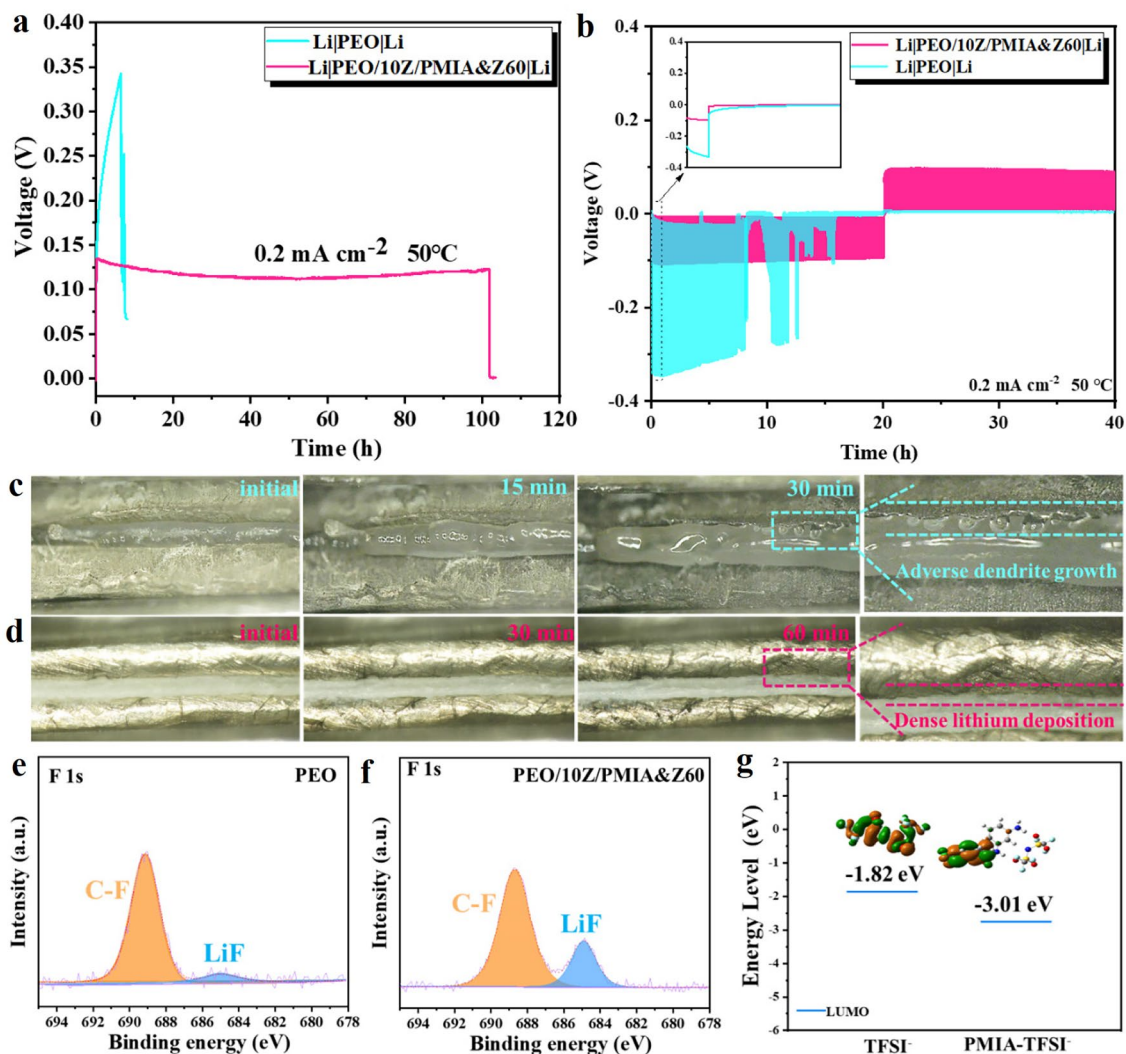
Fig. 6 **a** Galvanostatic charging tests and **b** Voltage profiles of GITT measurement for Li/Li cells with PEO and PEO/10Z/PMIA&Z60 SPEs under 0.2 mA cm^{-2} and 50 °C. (Inset: magnified voltage profiles to see the overpotential difference). In situ, in operando observation of dendrite suppression at the cross-sectional interface between electrolyte and lithium metal of **c** Li|PEO|Li and **d** Li|PEO/10Z/ PMIA&Z60|Li symmetric cells. (The cells continuously plated lithium at one interface testing at the current density of 0.2 mA cm^{-2} at 50 °C). High-resolution XPS spectra of F 1 s of **e** PEO and **f** PEO/10Z/PMIA&Z60 SPEs on the Li anode side. **g** LUMO levels of TFSI$^-$ and LUMO levels under hydrogen bonding

effectively increased the ionic conductivity and Li$^+$ transfer number of CSEs, which significantly inhibited the growth of lithium dendrites and homogeneous lithium deposition.

Figure S11 illustrates the surface conditions of the lithium anode after Li|SPEs|Li cycling. The SEM image of the lithium metal sheets of Li|PEO/10Z/PMIA&Z60|Li and Li|PEO/PMIA&L60|Li batteries both displayed smooth surfaces, indicating that effective inhibition of Li dendrite growth can be realized. However, the lithium anode of the Li|PEO|Li battery exhibited obvious mossy-like lithium dendrites, manifesting that uneven lithium deposition in the SPE and unstable interfaces can be formed between the SPE and the lithium anode.

The superior performance of Li||Li cells with PEO/10Z/ PMIA&Z60 and PEO/PMIA&L60 CSEs was mainly due to the outstanding ionic conductivity and the homogeneous Li$^+$ fluxes provided by the FICNFs networks. In addition, the nanoscale porosity of the PMIA nanofibers with excellent mechanical properties eliminated the "weak link" for micron-scale lithium dendrites to penetrate the applied membrane. More importantly, the hydrogen bond between the -NH groups in PMIA and TFSI$^-$ may cause the decomposition of CF$_3$ to produce CF$_2$ and LiF. That is, the LiF-rich SEI is formed, thereby promoting the uniform deposition/ detachment of lithium [49, 50]. To further demonstrate this conclusion, the composition of SEI formed in electrolytes

was studied using an X-ray photoelectron spectroscopy (XPS) test. After the Li|SPE|Li half cells for 50 cycles, the LiF-rich SEI can be formed on Li metal. As shown in Fig. 6e, f, the observed binding energies of the F1s spectra at 684.5 and 688.7 eV can be attributed to LiF and C–F, respectively. The binding energy of LiF can be formed in the prepared Li/PEO/10Z/PMIA&Z60 is higher than that of Li/PEO, which may result from the decompositions of LiTFSI during repeated charging and discharging processes. This was mainly explained by the hydrogen bonds between the –NH groups in PMIA and the TFSI$^-$ reduced the LUMO (lowest unoccupied molecular orbital) level of TFSI$^-$ from – 1.82 eV to – 3.01 eV as shown in Fig. 6g, which can effectively enhance the formation of robust LiF-rich SEI [51]. In conclusion, the synergistic effect between FICNFs and PMIA nanofibers enabled the Li|CSEs|Li batteries to have excellent cycling stability.

For the sake of investigating the performance of different electrolytes in full battery configuration, the Li|SPEs|LiFePO$_4$ (LFP) cells using the prepared

electrolytes were fabricated and tested (Fig. 7). Figure 7a displays the specific discharge capacities of Li||LFP cells from 0.1 C to 1 C. It was obvious that the assembled battery with PEO/10Z, PEO/PMIA, PEO/10Z/PMIA&Z60, and PEO/PMIA&L60 CSEs all exhibited a higher capacity at various current densities when compared with pure PEO SPEs, especially at a larger rate. Among them, the PEO/10Z/PMIA&Z60 and PEO/PMIA&L60 CSEs also displayed outstanding rate recovery performance. The discharge-specific capacities of PEO/10Z/PMIA&Z60 CSEs were 161.43 mAh g^{-1}, 154.85 mAh g^{-1} 150.82 mAh g^{-1} and 147.21 mAh g^{-1} at 0.1 C, 0.2 C, 0.5 C, and 1 C, respectively. Figures 7b and S12 display the smooth charge/discharge profiles of the Li| CSEs |LFP cell at different current densities, revealing the intimate contact of the two CSEs and electrodes. To fully evaluate the limits of PEO/10Z/PMIA&Z60 CSEs' rate capability, the Li|PEO/10Z/PMIA&Z60|LFP cells were tested at higher rates (3 C), which also presented outstanding rate recovery performance (Fig. S13).
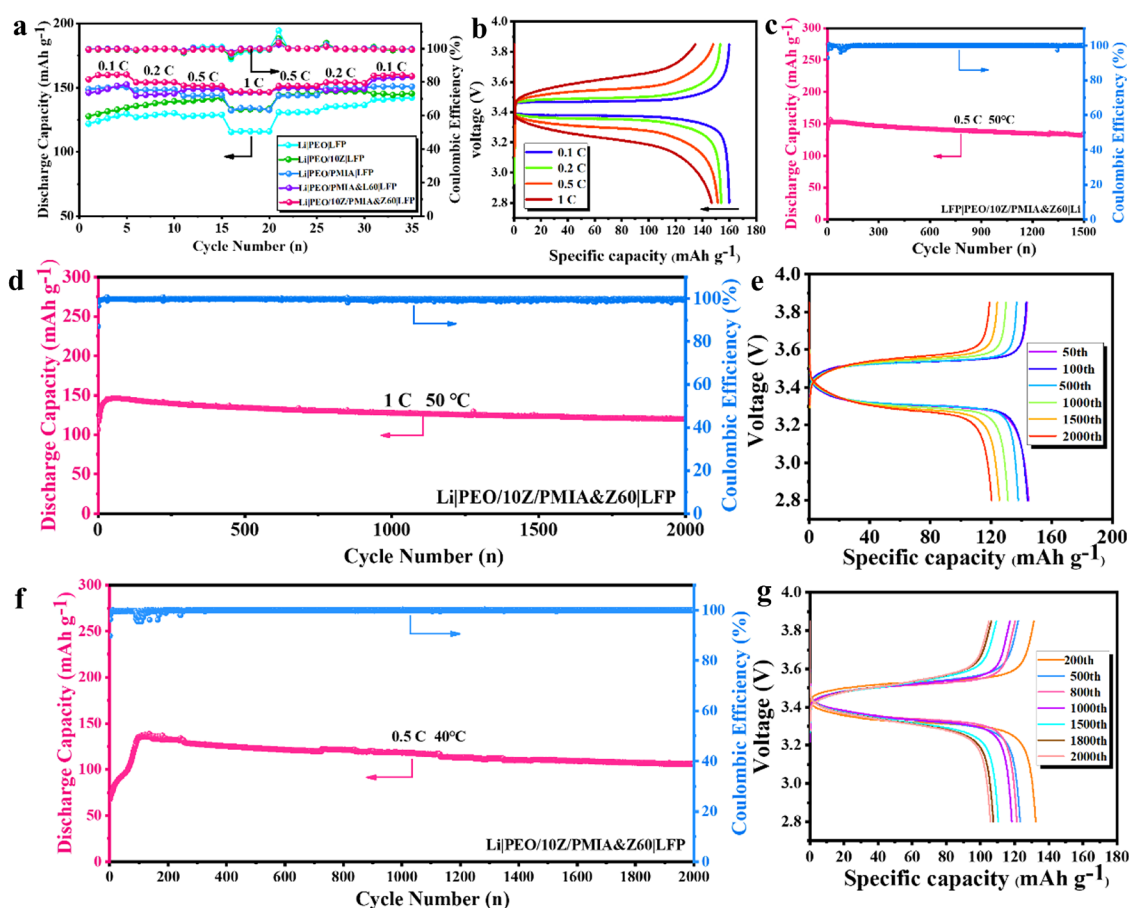

Fig. 7 **a** Rate performance of Li||LFP cells from 0.1 C to 1 C at 50 °C. **b** Charge–discharge voltage profiles of Li|PEO/10Z/PMIA&Z60|LFP cells at different rates. **c** Cycling performance of Li |PEO/10Z/PMIA&Z60|LFP at 0.5 C and 50 °C. **d** Cycling performance and **e** charge–discharge voltage profiles of Li|PEO/10Z/PMIA&Z60|LFP at 1 C and 50 °C. **f** Cycling performance and **g** charge–discharge voltage profiles of Li|PEO/10Z/PMIA&Z60|LFP at 0.5 C and 40 °C

Cycling tests of the Li‖LFP cells were also performed at 0.5 C and 1 C (50 °C) to examine their long-term stabilities. As shown in Fig. 7c, the Li‖LFP cell with the PEO/10Z/PMIA&Z60 CSE exhibited very stable cycling at 0.5 C. Notably, the discharge capacity of the Li‖LFP cells assembled with PEO/10Z/PMIA&Z60 CSEs was gradually increased at an early stage, which may be explained by the uniform distribution of lithium-ions and the gradual construction of lithium-ions transport channels in CSEs, as well as the improved surface contact between the CSEs and the electrodes [52, 53]. After the rising stage, the Li|PEO/10Z/PMIA&Z60|LFP cell reached a high discharge capacity of 157.6 mAh g^{-1} and remained at 132.5 mAh g^{-1} with an average Coulombic efficiency (CE) of 99.8% even after 1500 cycles. The charge/discharge profiles of the PEO/10Z/PMIA&Z60 CSEs battery under 0.5 C and 50 °C after different cycles are shown in Fig. S14, which displayed a smooth charging and discharging platform, illustrating that the long-term effectiveness of the battery interface can be obtained. The assembled Li‖LFP cell using PEO/PMIA&L60 CSEs also revealed a stable cycling performance, which displayed the discharge specific capacities of 129.2 mAh g^{-1} with average Coulombic efficiency (CE) of 99.8% and presented a smooth charging/discharging platform after 1500 cycles at 0.5 C (Figs. S15 and S16). Furthermore, the PEO/PMIA CSEs showed relatively satisfactory cycle performance, which had a 70.66% capacity retention rate after 980 cycles. Nonetheless, compared with the Coulomb efficiency exaggerated fluctuation just appeared after 400 stable cycles of PEO/10Z CSEs, the Coulombic efficiency of PEO SPEs fluctuated significantly and was very low only after 70 cycles. The remarkable cycling performance of Li‖LFP cells assembled with PEO/10Z/PMIA&Z60 and PEO/PMIA&L60 CSEs can be summarized for the following four reasons: (1) the FICNFs can provide multiple continuous transmission channels for Li$^+$, thus effectively improving the ionic conductivity of the composite electrolyte; (2) the applied TFSI$^-$ anion transport was limited by strong cationic sites on the surfaces of ZrO$_2$ and LLZTO, resulting in uniform Li$^+$ fluxes and high Li$^+$ transfer numbers; (3) the multiple hydrogen bond interactions in the electrolyte can effectively promote the dissociation of lithium salts and the formation of LiF-rich SEI; and (4) the PMIA nanofiber membrane made the electrolyte strongly resistant to the penetration of lithium dendrites, so the assembled lithium battery had excellent cycling stability.

Figure 7d further shows the cycling performance of Li‖LFP cells assembled with PEO/10Z/PMIA&Z60 CSEs at a higher rate of 1 C. Obviously, the PEO/10Z/PMIA&Z60 CSEs can sustain a specific capacity of 120.2 mAh g^{-1} even after 2000 cycles, and the battery also displayed high Coulomb efficiency and smooth charging and discharging platform (Fig. 7e). To demonstrate the multiple lithium-ion transport channels in the PEO/10Z/PMIA&Z60 CSEs, as well as its usability at low temperatures. The cycling performance of Li|PEO/10Z/PMIA&Z60|LFP was also tested at lower temperatures (40 °C) as shown in Fig. 7f and g, which maintained a stable discharge capacity of 118.4 mAh g^{-1} even after 2000 cycles with average CE of 99.8%.

The wide use of PEO-based solid-state electrolytes is limited in applications with lower voltage cathodes, such as LFP [54], due to their gradual oxidation at voltages above 3.9 V. The design of multiple Li$^+$ transport channels and hydrogen bonding enhanced solid-state electrolytes can effectively improve the electrochemical stability window of CSEs, resulting in excellent interfacial stability with the cell cathode. For further confirming the functionality of the PEO/10Z/PMIA&Z60 and PEO/PMIA&L60 CSEs described above, the Li‖NMC811 cells with both CSEs were also assembled to explore their compatibilities with the high-voltage cathodes. The EIS in Fig. 8a displays that when compared to pure PEO, the prepared PEO/10Z/PMIA&Z60 and PEO/PMIA&L60 CSEs have more prominent compatibility with high-voltage cathodes and lithium metals, which mainly contributes to the efficient operation of solid-state batteries. To verify the oxidation stability of two optimized CSEs in high-voltage cathode NMC811 batteries, we also have conducted electrochemical flotation experiments on different electrolytes. Among them, continue for 10 h within each incremental voltage to observe the current response. As shown in Fig. 8b, when the PEO/LiTFSI SPE was charged at a constant voltage of 4.2 V, the current seriously fluctuated. However, the current of the PEO/10Z/PMIA&Z60 and PEO/PMIA&L60 CSEs can remain stable in the range of 4.2–4.6 V, demonstrating excellent electrochemical stability. Figures 8c and S17–18 also present the rate capability of Li‖NMC811 cells with the two modified CSEs at various rates (0.1 C, 0.3 C, and 0.5 C). The test results show that the PEO/10Z/PMIA&Z60 and PEO/PMIA&L60 CSEs both have excellent discharge capacity, high average coulomb efficiency, and outstanding rate recovery performance at different rates. The smooth charging and discharging platform also demonstrated the intimate contact between the CSEs and the cathode. Besides, the electrochemical performance of Li|PEO/10Z/PMIA&Z60|NMC811 cell at 0.3 C is illustrated in Fig. 8d, e, which had a discharge capacity of 108.7 mAh g^{-1} even after 500 cycles at 0.3 C. In particular, the average CE of Li|PEO/10Z/PMIA&Z60|NMC811 cells can maintain around 99.6% during the whole cycle. The Li|PEO/PMIA&L60|NMC811 cell also can cycle stably after 100 cycles with an excellent average CE (Fig. S19). The good interfacial compatibility between the CSEs and high-voltage cathodes can be attributed to their wide electrochemical stability window and uniform lithium-ion transport, which enabled them to well match high-voltage electrode materials and further improve the mass-energy density.
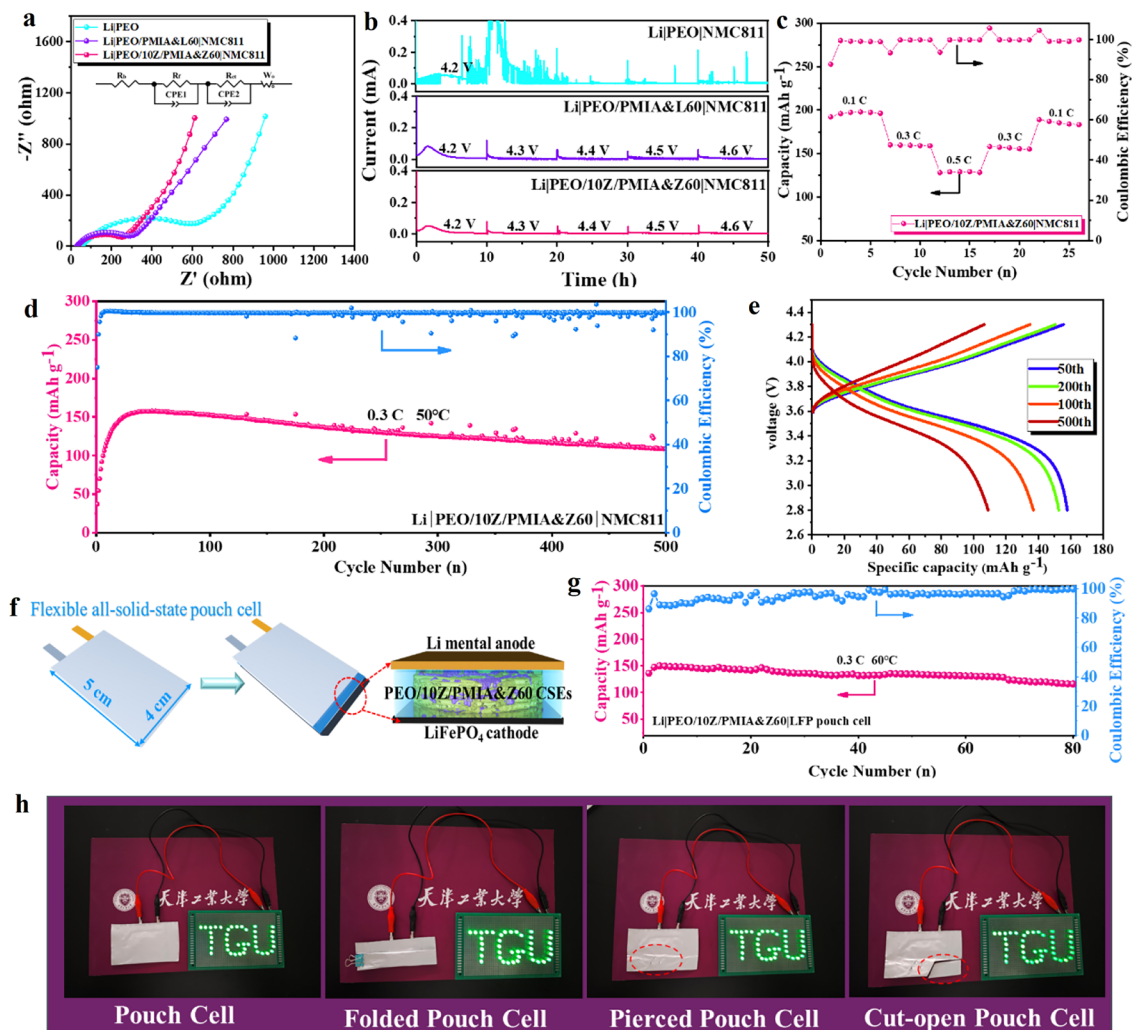
Fig. 8 **a** Electrochemical impedance spectra and **b** Electrochemical floating analysis of NMC811‖Li batteries with different electrolytes at 50 °C. **c** Rate performance of Li|PEO/10Z/PMIA&Z60|NMC811 cell from 0.1 C to 0.5 C at 50 °C. **d** Cycling performance and **e** charge–discharge voltage profiles of Li|PEO/10Z/PMIA&Z60|NMC811 at 0.3 C and 50 °C. **f** Schematic diagram of the pouch-type ASSLMBs. **g** Cycling performance of Li|PEO/10Z/PMIA&Z60|LFP pouch cell at 0.3 C and 60 °C. **h** The reliability and safety of the Li|PEO/10Z/PMIA&Z60|LFP pouch cell under normal, folding, punching, and cutting conditions

To investigate the practical application of PEO/10Z/PMIA&Z60 CSE in flexible electronic devices, we also designed a Li|PEO/10Z/PMIA&Z60|LFP pouch cell to demonstrate its functionality. Figure 8f illustrates the internal schematic diagram of the soft-pack ASSLMB. The cycle performance of the Li|PEO/10Z/PMIA&Z60|LFP pouch cell at 60 °C is depicted in Fig. 8g. The pouch cell exhibited stable cycling performance even after 80 cycles at 0.3 C and 60 °C, indicating a promising outlook for commercial utilization. Figure S20 illustrates the voltage profiles of the soft-pack ASSLMBs after various cycles at a rate of 0.3 C. It was noteworthy that no polarization effect was observed even after 80 cycles. Furthermore, the flexibility of the pouch-type ASSLMB was evaluated

under various conditions. As shown in Fig. 8h, the ultrathin Li|PEO/10Z/PMIA&Z60|LFP pouch cell, measuring 4 cm × 5 cm, was able to light 41 LED bulbs with a total rated power of 2.46 W at room temperature. Notably, those bulbs remained lit even under folding, piercing, and cutting. The remarkable safety performance can be attributed to the PEO/10Z/PMIA&Z60 CSE, known for their mechanical stability and flame resistance, which can significantly contribute to the overall safety of ASSLMBs.

All in all, through using the prepared composite electrolyte, the electrochemical performance of Li‖LFP and Li symmetrical cells all can obtain great improvement, illustrating that the ASSLMBs have entered the ranks of high-performance lithium batteries (Table S1).

Conclusions

In summary, novel multiple Li^+ transport channels and hydrogen bonding-enhanced CSEs were prepared for ASSLMBs by constructing FICNFs (with PEO as a binder to bind ZrO_2 or $Li_{6.4}La_3Zr_{1.4}Ta_{0.6}O_{12}$ nanoparticles) and PMIA nanofibers via scalable electrospinning and then backfilling with PEO/LiTFSI via solution casting. Basic characterization, electrochemical measurements, and related theoretical calculations, including DFT and AIMD simulations, demonstrated that the FICNFs and the PMIA nanofibers established many continuous, rapid Li^+ conduction pathways inside CSEs and adsorbed $TFSI^-$ to cause LiTFSI dissociation. In addition, the PMIA nanofibers improved the mechanical properties and thermal stabilities of the CSEs and caused the formation of a LiF-rich SEI. Therefore, the PEO/10Z/PMIA&Z60 and PEO/PMIA&L60 CSEs exhibited excellent abilities to inhibit the growth of lithium dendrites and good interfacial compatibilities with the $LiFePO_4$ cathode and the NMC811 high-voltage cathode at 50 °C. In particular, the Li|PEO/10Z/PMIA&Z60|LFP CSEs underwent ultralong stable cycling (> 2000 cycles) at 0.5 C and 40 °C. Moreover, the prepared CSEs displayed potential for use in flexible pouch batteries. This work mainly solves the problems of low ion conductivity, poor mechanical and thermal stability, weak ability to suppress lithium dendrites, narrow electrochemical window, and poor long-term stability of PEO-based electrolytes simultaneously, which provides an effective technical means for preparing SPEs with good electrochemical stability, high-temperature resistance, and safety.

Declarations

References

1. Cheng X-B, Zhao C-Z, Yao Y-X, Liu H, Zhang Q. Recent advances in energy chemistry between solid-state electrolyte and safe lithium-metal anodes. *Chem*. **2019**;*5*:74–96.

2. Zhou L, Tufail MK, Liao Y, Ahmad N, Yu P, Song T, Chen R, Yang W. Tailored carrier transport path by interpenetrating networks in cathode composite for high performance all-solid-state Li–SeS$_2$ batteries. *Adv Fiber Mater*. **2022**;*4*:487–502.

3. Wang Z, Shen L, Deng S, Cui P, Yao X. 10 μm-thick high-strength solid polymer electrolytes with excellent interface compatibility for flexible all-solid-state lithium-metal batteries. *Adv Mater*. **2021**;*33*:2100353.

4. Zhao W, Yi J, He P, Zhou H. Solid-state electrolytes for lithium-ion batteries: fundamentals, challenges and perspectives. *Electrochem Energy Rev*. **2019**;*2*:574–605.

5. Zhang Z, Huang Y, Gao H, Hang J, Li C, Liu P. MOF-derived ionic conductor enhancing polymer electrolytes with superior electrochemical performances for all solid lithium metal batteries. *J Membr Sci*. **2020**;*598*: 117800.

6. Culver SP, Koerver R, Krauskopf T, Zeier WG. Designing ionic conductors: the interplay between structural phenomena and interfaces in thiophosphate-based solid-state batteries. *Chem Mater*. **2018**;*30*:4179–92.

7. Guo Q, Xu F, Shen L, Deng S, Wang Z, Li M, Yao X. 20 μm-Thick Li$_{6.4}$La$_3$Zr$_{1.4}$Ta$_{0.6}$O$_{12}$-based flexible solid electrolytes for all-solid-state lithium batteries. *Energy Mater Adv*. **2022**. https://doi.org/10.34133/2022/975350.

8. Famprikis T, Canepa P, Dawson JA, Islam MS, Masquelier C. Fundamentals of inorganic solid-state electrolytes for batteries. *Nat Mater*. **2019**;*18*:1278–91.

9. Kato Y, Hori S, Saito T, Suzuki K, Hirayama M, Mitsui A, Yonemura M, Iba H, Kanno R. High-power all-solid-state batteries using sulfide superionic conductors. *Nat Energy*. **2016**;*1*:16030.

10. Li Z, Fu J, Zhou X, Gui S, Wei L, Yang H, Li H, Guo X. Ionic conduction in polymer-based solid electrolytes. *Adv Sci*. **2023**;*10*:2201718.

11. Xu F, Deng S, Guo Q, Zhou D, Yao X. Quasi-ionic liquid enabling single-phase poly(vinylidene fluoride)-based polymer electrolytes for solid-state LiNi$_{0.6}$Co$_{0.2}$Mn$_{0.2}$O$_2$||Li batteries with rigid-flexible coupling interphase. *Small Methods*. **2021**;*5*:2100262.

12. Ju J, Wang Y, Chen B, Ma J, Dong S, Chai J, Qu H, Cui L, Wu X, Cui G. Integrated interface strategy toward room temperature solid-state lithium batteries. *ACS Appl Mater Interfaces*. **2018**;*10*:13588–97.

13. Li C, Huang Y, Feng X, Zhang Z, Liu P. High electrochemical performance poly(ethylene oxide)/2,4-toluene diisocyante/polyethylene glycol as electrolytes for all-solid-state lithium batteries. *J Membr Sci*. **2019**;*587*: 117179.

14. Guo Q, Xu F, Shen L, Wang Z, Wang J, He H, Yao X. Poly(ethylene glycol) brush on Li$_{6.4}$La$_3$Zr$_{1.4}$Ta$_{0.6}$O$_{12}$ towards intimate interfacial compatibility in composite polymer

electrolyte for flexible all-solid-state lithium metal batteries. *J Power Sources*. **2021**;*498*: 229934.

15. Roman HE, Bunde A, Dieterich W. Conductivity of dispersed ionic conductors: a percolation model with two critical points. *PhRvB*. **1986**;*34*:3439–45.

16. Li Z, Huang H-M, Zhu J-K, Wu J-F, Yang H, Wei L, Guo X. Ionic conduction in composite polymer electrolytes: Case of PEO:Ga-LLZO composites. *ACS Appl Mater Interfaces*. **2019**;*11*:784–91.

17. Zheng J, Hu Y-Y. New insights into the compositional dependence of li-ion transport in polymer-ceramic composite electrolytes. *ACS Appl Mater Interfaces*. **2018**;*10*:4113–20.

18. Hu C, Shen Y, Shen M, Liu X, Chen H, Liu C, Kang T, Jin F, Li L, Li J, Li Y, Zhao N, Guo X, Lu W, Hu B, Chen L. Superionic conductors via bulk interfacial conduction. *J Am Chem Soc*. **2020**;*142*:18035–41.

19. Wang J, Yang J, Shen L, Guo Q, He H, Yao X. Synergistic effects of plasticizer and 3D framework toward high-performance solid polymer electrolyte for room-temperature solid-state lithium batteries. *ACS Appl Energy Mater*. **2021**;*4*:4129–37.

20. Zhang Z, Zhang Q, Ren C, Luo F, Ma Q, Hu Y-S, Zhou Z, Li H, Huang X, Chen L. A ceramic/polymer composite solid electrolyte for sodium batteries. *J Mater Chem A*. **2016**;*4*:15823–8.

21. Li Q, Sun X, Cao D, Wang Y, Luan P, Zhu H. Versatile electrospinning for structural designs and ionic conductor orientation in all-solid-state lithium batteries. *Electrochem Energy Rev*. **2022**;*5*:18.

22. Cheng H, Yan C, Orenstein R, Dirican M, Wei S, Subjalearndee N, Zhang X. Polyacrylonitrile nanofiber-reinforced flexible single-ion conducting polymer electrolyte for high-performance, room-temperature all-solid-state Li-metal batteries. *Adv Fiber Mater*. **2022**;*4*:532–46.

23. Wang Y, Wu L, Lin Z, Tang M, Ding P, Guo X, Zhang Z, Liu S, Wang B, Yin X, Chen Z, Amine K, Yu H. Hydrogen bonds enhanced composite polymer electrolyte for high-voltage cathode of solid-state lithium battery. *Nano Energy*. **2022**;*96*: 107105.

24. Zhang D, Liu Z, Wu Y, Ji S, Yuan Z, Liu J, Zhu M. In Situ Construction a stable protective layer in polymer electrolyte for ultralong lifespan solid-state lithium metal batteries. *Adv Sci (Weinh)*. **2022**;*9*: e2104277.

25. Park G, Lee K, Yoo D-J, Choi JW. Strategy for stable interface in lithium metal batteries: free solvent derived vs anion derived. *ACS Energy Lett*. **2022**;*7*:4274–81.

26. Tang S, Guo W, Fu Y. Advances in composite polymer electrolytes for lithium batteries and beyond. *Adv Energy Mater*. **2021**;*11*:2000802.

27. Li S, Zhang S-Q, Shen L, Liu Q, Ma J-B, Lv W, He Y-B, Yang Q-H. Progress and perspective of ceramic/polymer composite solid electrolytes for lithium batteries. *Adv Sci*. **2020**;*7*:1903088.

28. Miao X, Guan S, Ma C, Li L, Nan C-W. Role of interfaces in solid-state batteries. *Adv Mater*. **2023**;*35*:2206402.

29. Da X, Chen J, Qin Y, Zhao J, Jia X, Zhao Y, Deng X, Li Y, Gao N, Su Y, Rong Q, Kong X, Xiong J, Hu X, Ding S, Gao G. CO2-Assisted induced self-assembled aramid nanofiber aerogel composite solid polymer electrolyte for all-solid-state lithium-metal batteries. *Adv Energy Mater*. **2024**. https://doi.org/10.1002/aenm.202303527.

30. Liu W, Liu N, Sun J, Hsu P-C, Li Y, Lee H-W, Cui Y. Ionic conductivity enhancement of polymer electrolytes with ceramic nanowire fillers. *Nano Lett*. **2015**;*15*:2740–5.

31. Cai X, Ding J, Chi Z, Wang W, Wang D, Wang G. Rearrangement of ion transport path on nano-cross-linker for all-solid-state electrolyte with high room temperature ionic conductivity. *ACS Nano*. **2021**;*15*:20489–503.

32. Liu L, Lyu J, Mo J, Yan H, Xu L, Peng P, Li J, Jiang B, Chu L, Li M. Comprehensively-upgraded polymer electrolytes by multifunctional aramid nanofibers for stable all-solid-state Li-ion batteries. *Nano Energy*. **2020**;*69*: 104398.

33. Gao L, Liang H, Li J, Cheng B, Deng N, Kang W. The high-strength and ultra-thin composite electrolyte using one-step electrospinning/electrostatic spraying process for interface control in all-solid-state lithium metal battery. *J Power Sources*. **2021**;*515*: 230622.

34. Yue L, Ma J, Zhang J, Zhao J, Dong S, Liu Z, Cui G, Chen L. All solid-state polymer electrolytes for high-performance lithium ion batteries. *Energy Storage Mater*. **2016**;*5*:139–64.

35. Li Z, Wang S, Shi J, Liu Y, Zheng S, Zou H, Chen Y, Kuang W, Ding K, Chen L, Lan Y-q, Cai Y-p, Zheng Q. A 3D interconnected metal-organic framework-derived solid-state electrolyte for dendrite-free lithium metal battery. *Energy Storage Mater*. **2022**;*47*:262–70.

36. Li J, Zhang X, Lu Y, Linghu K, Wang C, Ma Z, He X. Electrospun fluorinated polyimide/polyvinylidene fluoride composite membranes with high thermal stability for lithium ion battery separator. *Adv Fiber Mater*. **2021**;*4*:108–18.

37. He A, Xing T, Liang Z, Luo Y, Zhang Y, Wang M, Huang Z, Bai J, Wu L, Shi Z, Zuo H, Zhang W, Chen F, Xu W. Advanced aramid fibrous materials: fundamentals, advances, and beyond. *Adv Fiber Mater*. **2023**. https://doi.org/10.1007/s42765-023-00332-1.

38. Liu K, Zhang R, Sun J, Wu M, Zhao T. Polyoxyethylene (PEO)|PEO–Perovskite|PEO composite electrolyte for all-solid-state lithium metal batteries. *ACS Appl Mater Interfaces*. **2019**;*11*:46930–7.

39. Xu R, Xiao Y, Zhang R, Cheng X-B, Zhao C-Z, Zhang X-Q, Yan C, Zhang Q, Huang J-Q. Dual-phase single-ion pathway interfaces for robust lithium metal in working batteries. *Adv Mater*. **2019**;*31*:1808392.

40. Hu J, Chen K, Yao Z, Li C. Unlocking solid-state conversion batteries reinforced by hierarchical microsphere stacked polymer electrolyte. *Sci Bull*. **2021**;*66*:694–707.

41. Lei M, Wu X, Liu Y, Chen K, Hu J, Li C. Polymer electrolytes reinforced by 2D fluorinated filler for all-solid-state Li–Fe–F conversion-type lithium metal batteries. *Nano Res*. **2023**;*16*:8469–77.

42. Chen H, Adekoya D, Hencz L, Ma J, Chen S, Yan C, Zhao H, Cui G, Zhang S. Stable seamless interfaces and rapid ionic conductivity of Ca–CeO$_2$/LiTFSI/PEO composite electrolyte for high-rate and high-voltage all-solid-state battery. *Adv Energy Mater*. **2020**;*10*:2000049.

43. Lin D, Liu W, Liu Y, Lee HR, Hsu P-C, Liu K, Cui Y. High ionic conductivity of composite solid polymer electrolyte via in situ synthesis of monodispersed SiO$_2$ nanospheres in poly(ethylene oxide). *Nano Lett*. **2016**;*16*:459–65.

44. Zhang X, Xie J, Shi F, Lin D, Liu Y, Liu W, Pei A, Gong Y, Wang H, Liu K, Xiang Y, Cui Y. Vertically aligned and continuous nanoscale ceramic-polymer interfaces in composite solid polymer electrolytes for enhanced ionic conductivity. *Nano Lett*. **2018**;*18*:3829–38.

45. Hatzell KB, Chen XC, Cobb CL, Dasgupta NP, Dixit MB, Marbella LE, McDowell MT, Mukherjee PP, Verma A, Viswanathan V, Westover AS, Zeier WG. Challenges in lithium metal anodes for solid-state batteries. *ACS Energy Lett*. **2020**;*5*:922–34.

46. Lu Y, Zhao C-Z, Yuan H, Cheng X-B, Huang J-Q, Zhang Q. Critical current density in solid-state lithium metal batteries: mechanism, influences, and strategies. *Adv Funct Mater*. **2021**;*31*:2009925.

47. Liu Y, Xu X, Kapitanova OO, Evdokimov PV, Song Z, Matic A, Xiong S. Electro-chemo-mechanical modeling of artificial solid electrolyte interphase to enable uniform electrodeposition of lithium metal anodes. *Adv Energy Mater*. **2022**;*12*:2103589.

48. Xu X, Liu Y, Kapitanova OO, Song Z, Sun J, Xiong S. Electro–chemo–mechanical failure of solid electrolytes induced by growth of internal lithium filaments. *Adv Mater*. **2022**;*34*:2207232.

49. Zhou X, Zhang B, Huang F, Li F, Ma Z, Liu J. Difunctional MOF for dendrite-free all-solid-state lithium metal batteries by synergistic effect of hydrogen bond and electrostatic interaction. *Nano Energy*. **2023**;*108*: 108221.

50. Zhou X, Li C, Zhang B, Huang F, Zhou P, Wang X, Ma Z. Difunctional NH2-modified MOF supporting plentiful ion channels and stable LiF-rich SEI construction via organocatalysis for all-solid-state lithium metal batteries. *J Mater Sci Technol*. **2023**;*136*:140–8.

51. Zhang X, Su Q, Du G, Xu B, Wang S, Chen Z, Wang L, Huang W, Pang H. Stabilizing solid-state lithium metal batteries through in situ generated Janus-heterarchical LiF-rich SEI in ionic liquid confined 3D MOF/polymer membranes. *Angew Chem Int Ed*. **2023**;*62*: e202304947.

52. Yan C, Zhu P, Jia H, Du Z, Zhu J, Orenstein R, Cheng H, Wu N, Dirican M, Zhang X. Garnet-rich composite solid electrolytes for dendrite-free, high-rate, solid-state lithium-metal batteries. *Energy Storage Mater*. **2020**;*26*:448–56.

53. Ma J-l, Meng F-l, Yu Y, Liu D-p, Yan J-m, Zhang Y, Zhang X-b, Jiang Q. Prevention of dendrite growth and volume expansion to give high-performance aprotic bimetallic Li–Na alloy–O2 batteries. *Nat Chem*. **2019**;*11*:64–70.

54. Zhou W, Wang Z, Pu Y, Li Y, Xin S, Li X, Chen J, Goodenough JB. Double-layer polymer electrolyte for high-voltage all-solid-state rechargeable batteries. *Adv Mater*. **2019**;*31*:1805574.